Deconvolution of adaptive optics images with imprecise knowledge of the point spread function: results on astronomical objects.*

Jean-Marc Conan, Thierry Fusco, Laurent M. Mugnier, Evy Kersalé and Vincent Michau

Office National d'Études et de Recherches Aérospatiales (ONERA)
Département d'Optique Théorique et Appliquée
BP 72, F-92322 Châtillon cedex, France
* Comments to: conan@onera.fr

Abstract The performance of high resolution imaging with large optical instruments is severely limited by the atmospheric turbulence. Adaptive optics offers a real time compensation of the turbulence. The correction is however only partial and the long exposure images must be deconvolved to restore the fine details of the object.

The "myopic" deconvolution scheme is briefly presented. This approach takes into account the noise in the image, the imprecise knowledge of the point spread function (PSF), and the available *a priori* information on the object (spatial structure, positivity...). The effect of seeing variations on the PSF estimation is discussed. Besides, a specific edge preserving object prior is proposed for the application to planetary-like objects.

The performance of the myopic deconvolution is illustrated on images of solar system objects recorded with the ONERA adaptive optics bench installed on the 1.52m telescope at Observatoire de Haute Provence.

Key words: adaptive optics, atmospheric turbulence, deconvolution, image restoration, inverse problems, astronomy.

1 Introduction

The performance of high resolution imaging with large optical instruments is severely limited by the atmospheric turbulence. In the past 20 years various techniques have been proposed to overcome this limitation and to effectively reach the diffraction limit of the telescopes. Speckle interferometry[1] was first proposed and is based on recording series of images with exposure times short enough to freeze the turbulence. Various numerical post-processing methods[2, 3, 4] then permit to reconstruction of the observed object. Alternatively, adaptive optics[5, 6] (AO) offers a real time compensation of the turbulence. One can therefore record long exposure images without losing the object high spatial frequencies corresponding to the fine details. The high spatial frequencies are not lost but they can however be severely attenuated since the correction is often only partial[6, 7, 8, 9, 10]. Consequently, the AO corrected long exposure images must be deconvolved to properly restore the object. A common feature of techniques for imaging through turbulence is that the PSF is not known accurately, which makes deconvolution more difficult.

The goal of this paper is to apply a deconvolution scheme based on a maximum *a posteriori* approach to AO corrected astronomical images. This approach takes into account the noise in the image and the *a priori* information on the object to be restored, as well as the imprecise knowledge of the PSF. The data processed here correspond to solar system objects, the object prior is therefore enforced by means of an appropriate edge preserving regularization function.

The problem of the deconvolution of AO images is presented in Section 2. Our approach to the classical and myopic deconvolution is described in Section 3. Finally, the deconvolution technique is applied to experimental data and the results are presented in Section 4.

2 Partially Corrected AO Images

Within the isoplanatic angle, the intensity $\mathbf{i}(r)$ at the focal plane of the system consisting of the atmosphere, of the telescope and of the AO bench is given by:

$$\mathbf{i}(r) = \mathbf{h}(r) \star \mathbf{o}(r) + \mathbf{n}(r) \tag{1}$$

where r is the spatial coordinate, $\mathbf{o}(r)$ is the observed object, $\mathbf{h}(r)$ is the system Point Spread Function (PSF) and $\mathbf{n}(r)$ is an additive zero mean noise. We consider here the case of AO corrected long exposure images. The AO

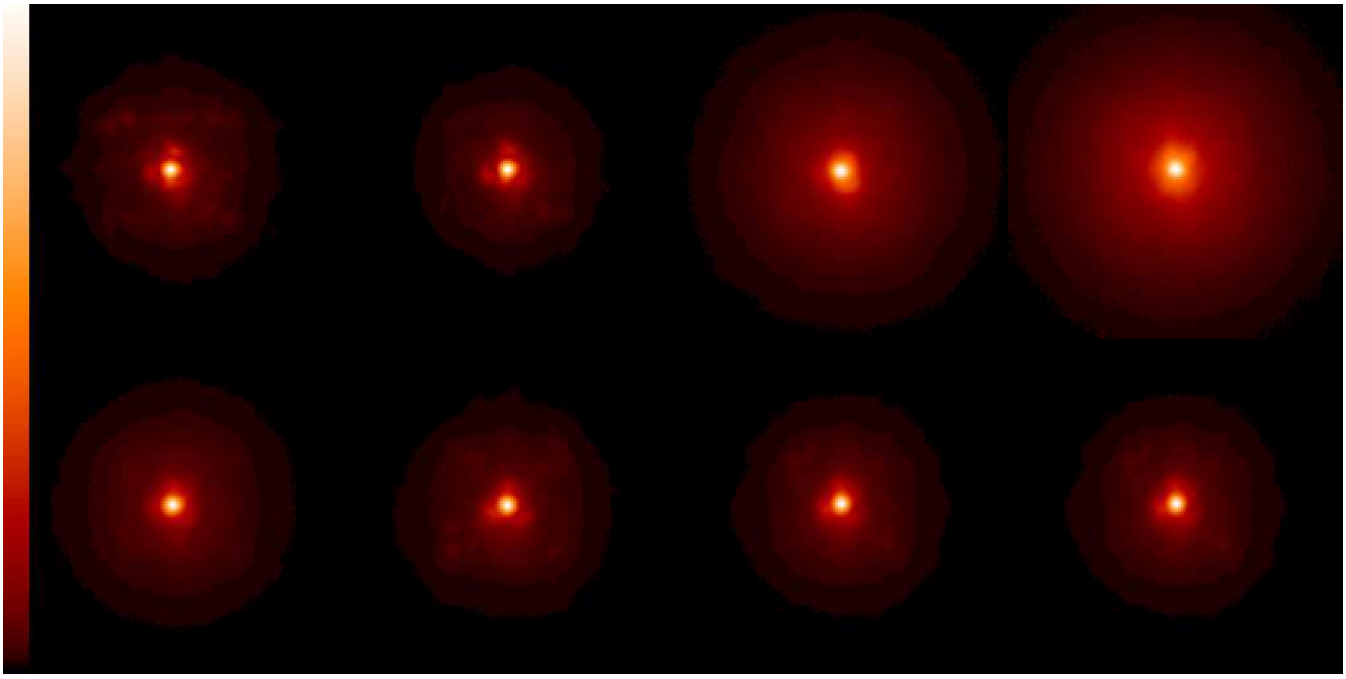

Figure 1: Experimental images of a star (63 Ceti) obtained on ONERA's AO bench on 1997/09/28 at 00h05, 00h39, 01h05, 01h31, 02h02, 02h28, 02h54 UT, respectively. The corresponding estimated Strehl ratios are: $8.4, 9.8, 3.6, 2.3, 6.7, 8.0$ *and* 7.9% with an estimated average D/r_o of 25 at the observing wavelength 850 nm. The field of view is 3.47 arcsec (128×128 pixels) and the exposure time 5 min.

correction is however only partial and the corrected image must be deconvolved to restore the fine details of the observed object. The deconvolution quality is improved when a measure of the PSF is available. The usual procedure therefore consists in recording the corrected image of a nearby unresolved star shortly after observing the object of interest. Since the correction quality depends on the observing conditions (turbulence strength, magnitude of the source used for wavefront sensing), the unresolved star image is not a perfect measure of the PSF associated with the image to be deconvolved[11, 12]. Actually the main source of PSF variability is the seeing fluctuation. This is illustrated in Fig. 1 which shows 7 experimental images of a star (63 Ceti, of magnitude $M_v = 5.9$). These 5 minute exposure images were recorded with approximately a 30 minute interval between them. The imaging wavelength is 850 nm ($40nm$ spectral bandwidth). The correction quality is highly variable, the Strehl Ratio ranges here from 2 to 10%.

These images, as well as all the other experimental data presented in this paper, were obtained on ONERA's AO bench at the 1.52 m telescope of Observatoire de Haute Provence. This bench has the following characteristics: it is equipped with a 10×10 piezo-stack mirror (of which 88 actuators are active). It uses a 9×9 subaperture Shack-Hartmann wavefront sensor, with 64 useful subapertures. The AO maximum servo-loop bandwidth is 80 Hz.

The long exposure Optical Transfer Function (OTF) corresponding to the first image of 63 Ceti is shown in Fig. 2. This is a typical corrected OTF[7, 8, 9, 10]: a low frequency lobe and a high frequency wing going up to the telescope cutoff frequency. The spatial frequencies between r_o/λ and D/λ, which would be lost without correction,

are now preserved although severely attenuated. Note that the images are oversampled at this wavelength. The image scale is 27.3 marcsec/pixel. This value is estimated on a calibration star (ζ Aqr) using a specific multiple star deconvolution scheme[13].

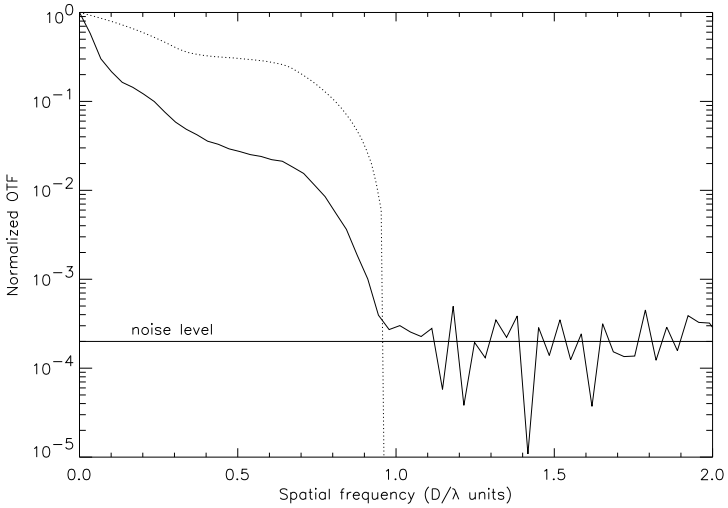

Figure 2: Normalized optical transfer function versus spatial frequency: AO corrected OTF corresponding to the first image of 63 Ceti shown in Fig. 1 (solid line). The aberration free OTF (dotted line) is shown for comparison. The spatial frequency is normalized to the telescope cutoff.

63 Ceti was actually taken as a reference star for observations of the asteroid Vesta ($M_v = 6.6$) located 3 degrees apart. Since the star was slightly brighter than Vesta a neutral density was added on the wavefront sensing channel to ensure a similar correction quality on both objects. Vesta was observed 8 times during that part of the night. These 5 minute exposures are shown Fig. 3. Vesta's revolution is 5.34 hours[14], the image sequence shown in Fig. 3 therefore corresponds to slightly more than half a revolution. However, no evidence of the rotation is seen on these images. Due to the partial correction no details or edges can be seen on any image. Additionally the changes between images are dominated by the correction quality variability rather than by a change in the object aspect. The goal of this paper is to present a deconvolution scheme able to process such a data set (astronomical object and associated unresolved star images) accounting for the image noise and the PSF variability in order to properly restore the high spatial frequencies of the object. This is of course particularly important for a fine astronomical study (rotation, shape, photometry on the surface structures ...).

After a brief review of various deconvolution approaches with a known PSF in Sect. 3.1, we propose an edge preserving prior for planetary objects (see Sect. 3.2). Section 3.3 presents our myopic deconvolution scheme which accounts for the PSF variability. The myopic deconvolution is then applied to images of Vesta and Ganymede, the results are shown in Sect. 4.

3 Deconvolution Approach

Most deconvolution techniques boil down to the minimization (or maximization) of a criterion. The first issue is the definition of a suitable criterion for the given inverse problem. The criteria presented here will be derived from a stochastic approach (maximum likelihood [ML], maximum *a posteriori* [MAP]). The second problem is then to find the position of the criterion's global minimum which is defined as the solution. In some cases it is given by an analytical expression, but most of the time one has to use an iterative numerical method to solve the problem. The numerical method is efficient if it leads to the global minimum no matter what the starting point is. For our applications we use a conjugate gradient method. The efficiency of such a method will be discussed for the different criteria proposed here.

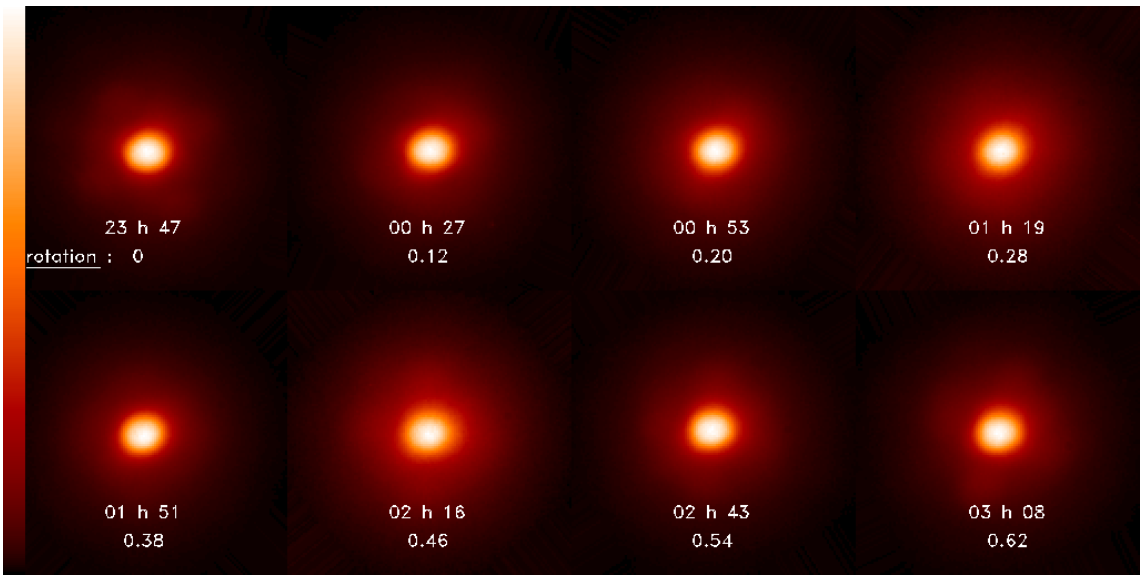

Figure 3: Corrected images of Vesta observed with ONERA's AO bench during the night 1997/09/27-28. The wavelength is $\lambda = 0.85\mu m$, the field of view 3.47 arcsec, the exposure time 5 min. and the estimated total flux $\approx 6.10^7 photons$.

In the following sections, we first consider the case of a assumedly known PSF referred to, in this paper, as "classical" deconvolution; the method is then extended to the joint estimation of the object and the PSF, called here "myopic" deconvolution.

3.1 Deconvolution with known PSF

It is now well known that the restoration of the object using the sole data is an unstable process (see in particular Refs. [15] and [16] for reviews). It is the case for the ML solution which corresponds to maximizing $p(\mathbf{i}|\mathbf{o})$, the probability of the image knowing the object, directly related to the noise statistics. With a white Gaussian noise this gives the least square solution (minimization of $J_{gauss}(\mathbf{o}) = \sum_r \frac{1.}{2\sigma^2(r)}(\mathbf{i}(r) - (\mathbf{o} \star \mathbf{h})(r))^2$). Furthermore, if the noise variance $\sigma^2(r)$ is assumed to be uniform, the minimization problem has an analytical solution which is the inverse filter ($\tilde{\hat{\mathbf{o}}}(f) = \tilde{\mathbf{i}}(f)/\tilde{\mathbf{h}}(f)$ where $\tilde{\cdot}$ denotes the Fourier transform and f the spatial frequency). Since the OTF $\tilde{\mathbf{h}}(f)$ is zero beyond the telescope cut-off frequency, the solution is clearly unstable, meaning that it leads to an uncontrolled amplification of the noise.

Similarly, the ML solution with photon noise (minimization of $J_{poisson}(\mathbf{o}) = \sum_r (\mathbf{h} \star \mathbf{o})(r) - \mathbf{i}(r) \ln[(\mathbf{h} \star \mathbf{o})(r)]$) is also unstable. Note, that the Richardson-Lucy[17, 18] algorithm [RL] is nothing but an iterative process which minimizes $J_{poisson}$. As an illustration, we apply RL to the first of Vesta's images shown in Fig. 3. The PSF is assumed to be the image of 63 Ceti acquired shortly after (first image of Fig. 1). The ML estimate is obtained for an infinite number of iterations but, as shown in Fig. 4, the object obtained for 50000 iterations is already very noisy. It is possible to limit the noise amplification by stopping the algorithm before convergence, but this leads to a poor control of the solution. The solution obtained for 1000 iterations is indeed smoother but it is difficult to tell whether it is a good restoration of the true object. In particular the bright and dark areas seen on the surface can be shown to be ringing effects due to a sharp cut-off in the object spectrum. This artifact is common for planetary like objects[19], and we will show how to avoid this problem by using an adequate object prior in Sect. 3.2.

In any case, the inverse problem must be regularized by the use of prior information on the solution; a new criterion to be minimized (or maximized) must be defined accordingly. We do so in a MAP framework: the object is endowed with an *a priori* distribution $p(\mathbf{o})$, and Bayes' rule combines the likelihood of the data $p(\mathbf{i}|\mathbf{o})$ with this *a priori* distribution into the *a posteriori* probability distribution $p(\mathbf{o}|\mathbf{i})$. If the PSF $\mathbf{h}$ is perfectly known, then the

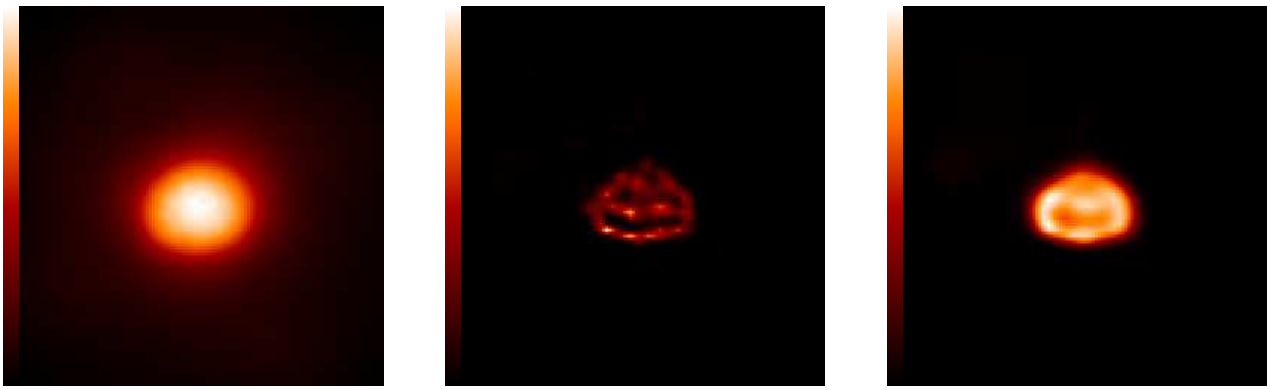

Corrected Image | Richardson-Lucy (50000 it.) | Richardson-Lucy (1000 it.)

Figure 4: Deconvolution of the first image of Vesta shown in Fig. 3 with the Richardson-Lucy algorithm for 50000 and 1000 iterations. The first image of 63 Ceti shown in Fig. 1 is used as the PSF.. The total field of view for the deconvolution is 3.47 arcsec but only the central 1.74 arcsec field of view is printed here.

restored object can be defined as the most probable one given the data:

$$\hat{\mathbf{o}}_{\text{map}} = \arg\max_{\mathbf{o}} p(\mathbf{o}|\mathbf{i}) = \arg\max_{\mathbf{o}} p(\mathbf{i}|\mathbf{o}) \times p(\mathbf{o}) = \arg\min_{\mathbf{o}} \left[J_n(\mathbf{o}) + J_o(\mathbf{o})\right]. \tag{2}$$

The criterion to be minimized, $J = J_n + J_o$, is composed of the opposite of the log-likelihood of the data (J_n) plus an object regularization term ($J_o = -\ln p(\mathbf{o})$). This last term of course is a function of the type of object being observed. The choice of J_o for planetary type objects is discussed in the following section.

In this paper J_n is a least square term (J_{gauss}) with a uniform noise variance equal to the mean number of photons per pixel. This can be considered as a first approximation of a photon noise in the case of a bright and rather extended object.

3.2 Edge preserving object prior

The use of Gaussian statistics for the object prior was shown to be efficient on smooth objects[20]. However such a prior forbids the restoration of sharp edges[21]. As a matter of fact, without additional constraints, the solution of Eq. 2 with a Gaussian prior has an analytical solution which is the Wiener filter[22]. Since the solution is a simple linear filter applied to the image, no spectrum extrapolation is possible beyond the telescope cut-off and sharp edges cannot be restored.

Several edge preserving priors have been proposed in the literature[21]. Here we use a $L_1 - L_2$ criterion, quadratic for small gradients and linear for large ones[23]. The quadratic part ensures a good smoothing of the small gradients (i.e. of noise), and the linear behavior cancels the penalization of large gradients (i.e. of edges)[24]. We propose an original function which is an isotropic version of the expression suggested by Brette[25]:

$$J_o(\mathbf{o}) = \mu \sum_r \left[\left(\frac{\Delta\mathbf{o}(r)}{\delta}\right) - \ln\left(1 + \frac{\Delta\mathbf{o}(r)}{\delta}\right)\right] \tag{3}$$

where $\Delta\mathbf{o}(r) = \sqrt{\Delta_x\mathbf{o}(r)^2 + \Delta_y\mathbf{o}(r)^2)}$, $\Delta_x\mathbf{o}$ and $\Delta_y\mathbf{o}$ are the object finite difference gradients along x and y respectively.

The global factor μ and the threshold δ have to be adjusted according to the noise level and the structure of the object. This is currently done by hand but an automatic procedure is under study. Note that this function is convex, as well as the global criterion, which justifies the use of a gradient-based method for the minimization.

This object prior is tested on simulated data and the results are shown in Fig. 5. The true object is a planetary-like object with sharp edges and bright area in the lower-left corner (7% contrast). The corrected PSF used in the simulation is the first image of 63 Ceti. Photon noise is added to the corrected image with a total flux

of 1.10^8 photons. This image is rather similar to the image recorded on Vesta. The object is restored by applying the edge preserving classical deconvolution scheme described above with an additional positivity constraint enforced with a reparametrization method ($\mathbf{o} = \mathbf{a^2}$)[26]. The true PSF is used here. The object contour and the bright spot are well restored. This result is compared to the Wiener filter restoration. As expected the sharp decrease of the object spectrum near the telescope cut-off induces smooth edges and strong ringing effects. This is particularly illustrative of the fact that a linear technique can give a very poor photometric accuracy compared to a non-linear one incorporating simple but pertinent prior information (see Fig. 6).

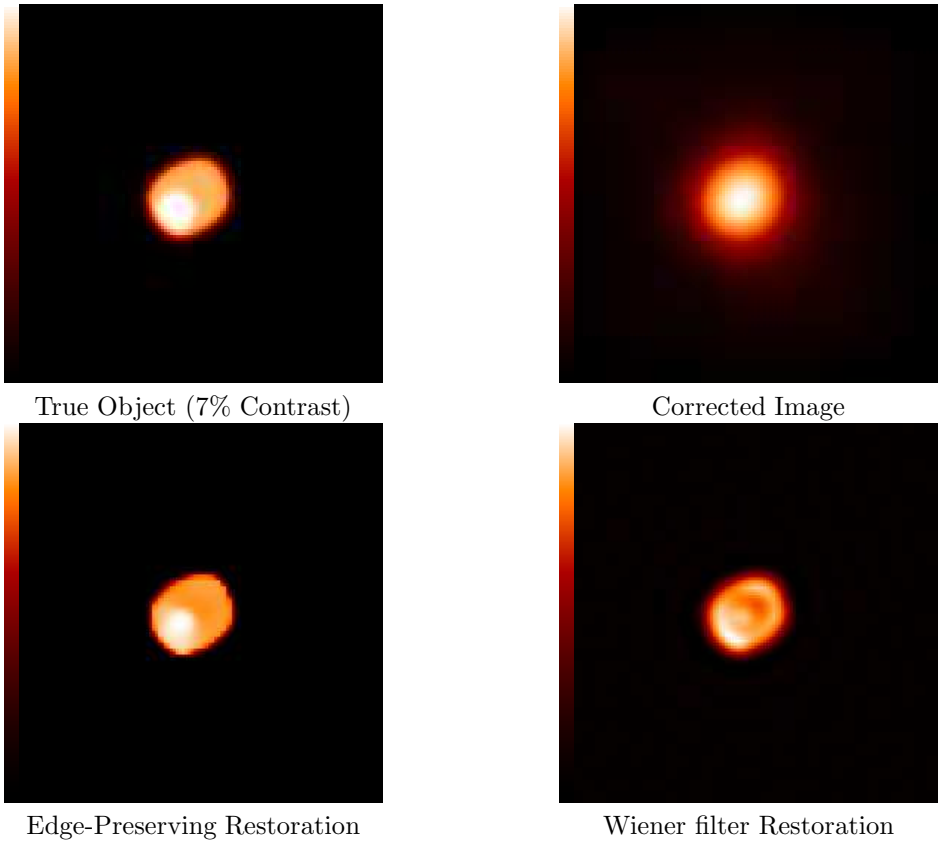

Figure 5: Deconvolution of the simulated image of a planetary-like object with known PSF. The corrected image is the convolution of the true object by the PSF, taken here as the first image of 63 Ceti shown in Fig. 1. Photon noise was added with a total flux of 1.10^8 photons. The edge preserving MAP restoration is compared to the Wiener filter solution. The total field of view for the deconvolution is 3.47 arcsec but only the central 1.74 arcsec field of view is printed here (64×64 pixels).

This simulation corresponds to the ideal case where the true PSF is perfectly known. As mentioned in Sect. 2 this is generally not the case. One can still use the classical deconvolution with an erroneous estimate of the true PSF, but we have shown that the PSF estimation errors lead to a severe deterioration of the object restoration[20]. It is therefore important to account for the PSF variability in the deconvolution process itself as proposed in Sect. 3.3.

3.3 Myopic deconvolution and PSF prior

Several authors have addressed this problem of deconvolution of turbulence degraded images with an unknown PSF. Ayers and Dainty[27] used a Gerchberg-Saxton-Papoulis[28, 29, 30] type algorithm, and encountered the known[31] convergence problems associated with such projection based algorithms. Others[32, 33, 34, 35, 26, 36, 37, 38] have used methods based on a ML approach, the algorithm used to maximize the likelihood being either the Expectation-Maximization method[32, 34] or the minimization of an explicit criterion[33, 35, 26, 36, 37, 38]. They have generally

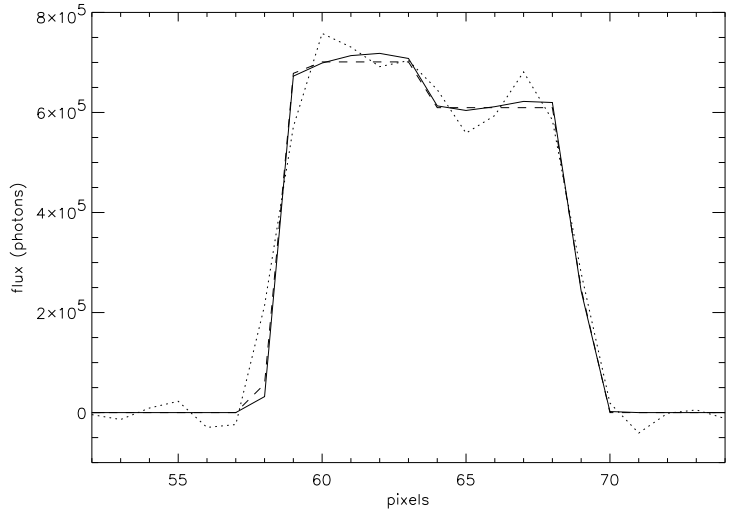

Figure 6: Profile of the object along the diagonal (lower left to upper right corner): true object (dashed line), Wiener filter estimate (dotted line) and edge preserving restoration (solid line).

recognized the need for a regularization other than the sole positivity (of the object and of the PSF), and introduced in particular a band-limitedness on the PSF[32, 35, 38].

This kind of *a priori* information on the solution (and more if it is available) can be introduced very easily by adopting the MAP approach for the joint estimation of the object and of the PSF[20, 11, 13]. Indeed, the PSF in the presence of turbulence can quite naturally be considered as a stochastic process. The estimator then becomes:

$$[\hat{\mathbf{o}}, \hat{\mathbf{h}}] = \arg\max_{\mathbf{o},\mathbf{h}} p(\mathbf{o}, \mathbf{h}|\mathbf{i}) = \arg\max_{\mathbf{o},\mathbf{h}} p(\mathbf{i}|\mathbf{o}, \mathbf{h}) \times p(\mathbf{h}) \times p(\mathbf{o}) = \arg\min_{\mathbf{o},\mathbf{h}} \left[J_n(\mathbf{o}, \mathbf{h}) + J_h(\mathbf{h}) + J_o(\mathbf{o})\right] \tag{4}$$

with a new criterion $J = J_n + J_h + J_o$ which is now a function of $\mathbf{o}$ and of $\mathbf{h}$ and which includes a PSF regularization term ($J_h = -\ln p(\mathbf{h})$) similarly to a recently suggested deterministic approach[39]. In the following applications, we also use positivity constraints for both the object and the PSF ($\mathbf{o} = \mathbf{a^2}$, $\mathbf{h} = \mathbf{b^2}$).

Assuming stationary Gaussian statistics for the PSF, J_h reads:

$$J_h(\mathbf{h}) = \frac{1}{2} \sum_f \frac{\left|\tilde{\mathbf{h}}(f) - \tilde{\mathbf{h}}_\mathbf{m}(f)\right|^2}{PSD_h(f)}, \tag{5}$$

where PSD_h is the spatial Power Spectral Density [PSD] of the PSF, and $\tilde{\mathbf{h}}_\mathbf{m} = E[\tilde{\mathbf{h}}]$ is the mean OTF (Fourier transform of the mean PSF). PSD_h is expressed simply as a function of the first two moments of the OTF:

$$PSD_h(f) = E[|\tilde{\mathbf{h}}(f) - \tilde{\mathbf{h}}_\mathbf{m}(f)|^2] = E[|\tilde{\mathbf{h}}(f)|^2] - |\tilde{\mathbf{h}}_\mathbf{m}(f)|^2. \tag{6}$$

Such a regularization obviously ensures that the actual PSF is close to the mean PSF with respect to error bars given by the PSD, which characterizes the PSF fluctuations around the mean. It should be noted that $PSD_h(f)$ is zero above the cutoff of the telescope, so that the regularization in particular enforces a band-limited constraint.

In practice, the mean PSF and the PSD are estimated by replacing, in their definitions, the expected values ($E[\cdot]$) by an average on the different images recorded on the unresolved star (see for instance Fig. 1). Ideally one would want to estimate the PSF from the wavefront sensing data[40] which would avoid the errors due to seeing fluctuations. But even in this case, the myopic approach can be interesting to account for the PSF uncertainties due to constant aberration calibration errors[13] or to the wavefront sensing noise for faint stars.

Note that the new criterion is convex in $\mathbf{o}$ for a given $\mathbf{h}$, convex in $\mathbf{h}$ for a given $\mathbf{o}$ but it is not convex on the whole parameter space. However it is possible to use starting points which are close to the global minimum (mean PSF and object solution of the classical deconvolution, for instance), and we did not encounter minimization problems with the conjugate gradient method.

4 Deconvolution of Experimental Data

4.1 Rotation of Vesta

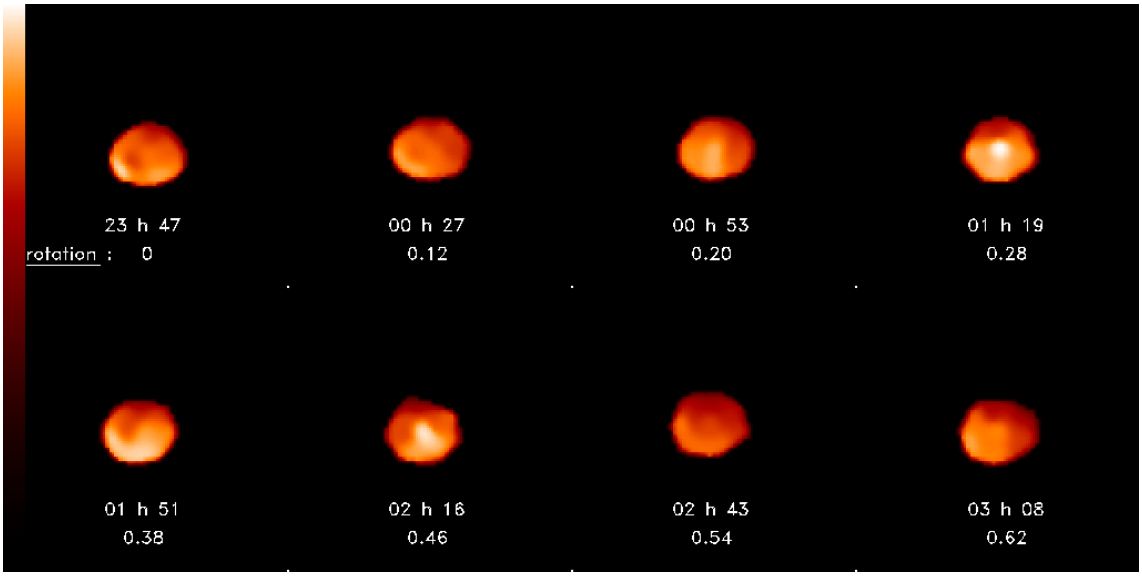

Figure 7: Edge preserving myopic deconvolution of the corrected images of Vesta shown in Fig. 3. Only the central 1.74 arcsec field of view is shown here.

The edge preserving myopic restoration described in Sect. 3 is applied to the corrected images shown in Fig. 3 and the results are shown in Fig. 7. In both figures the field rotation of the coudé focus was accounted for and all the images are oriented so that the rotation axis is vertical.

The contour is well restored and the evolution of the apparent surface gives a clear evidence of the rotation. This is confirmed by Fig. 8 which shows the apparent surface estimated by counting the number of pixels above a given threshold in the restored frames. Despite the small number of resolved points, structures denoting local albedo variations are seen on the surface[41, 42]. The time interval between two frames corresponds to ≈ 0.1 revolution ($\approx 36\,\mathrm{deg}$), the aspect therefore evolves quickly and the interpretation is not easy. Nonetheless, bright features can be often tracked on two successive frames. Besides, the intensity scale of Fig. 8 is not changed between frames, and one clearly notices that one side of the asteroid is brighter than the other. The maximum intensity occurs around 01:51 UT and also corresponds to Vesta showing its the smaller apparent surface. This behavior has been noted by Drummond[14] on observations made on 1996/05/11 (maximum flux around 10:00 UT). We have checked that there is an integer number of revolutions between the brightness maxima of these two observations, when accounting for the relative position of the Earth and Vesta.

Note also that the edge preserving regularization avoids the usual turned up edge artifacts (i.e. ringing) which usually makes the interpretation very difficult.

4.2 Observation of Ganymede

The satellite of Jupiter, Ganymede ($M_v = 4.6$, diam ≈ 1.7 arcsec), has been observed during the same observing run at the Observatoire de Haute Provence in particularly severe seeing conditions: $D/r_o \approx 23$ at the imaging wavelength $0.85\mu m$. The object itself is used for the wavefront sensing. The corrected image (100 sec. exposure time), recorded on 1997/09/28 at 20:18 UT, is shown in Fig. 9 and does not exhibit any detail. θ Cap ($M_v = 4.1$), located 1.5 degrees apart, was then observed as a PSF calibration at 22:24 UT. A neutral density was used to have approximately the same wavefront sensing conditions. The PSD and mean OTF are estimated on a series of 50 images recorded with an exposure time of 1 sec. The difference in exposure times between the reference star and Ganymede was accounted for in the PSD calculation[20]. The RL algorithm is applied to the corrected image using

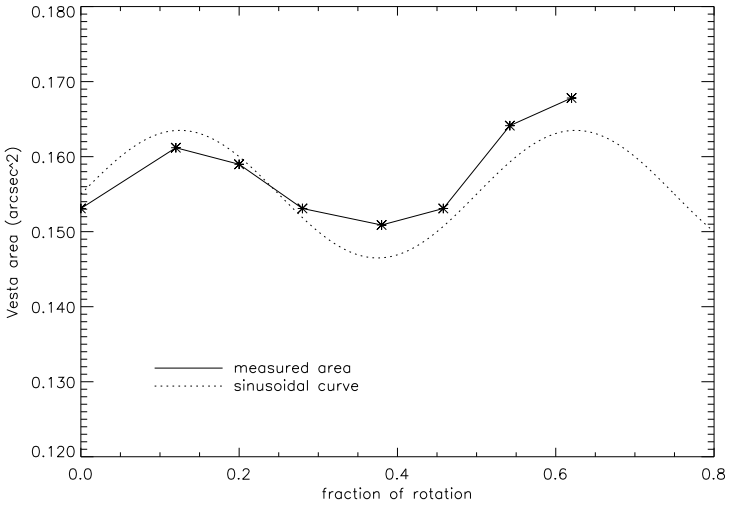

Figure 8: Evolution of the apparent surface of Vesta estimated from the deconvolved images. A sine wave with a period of half the revolution is plotted for comparison.

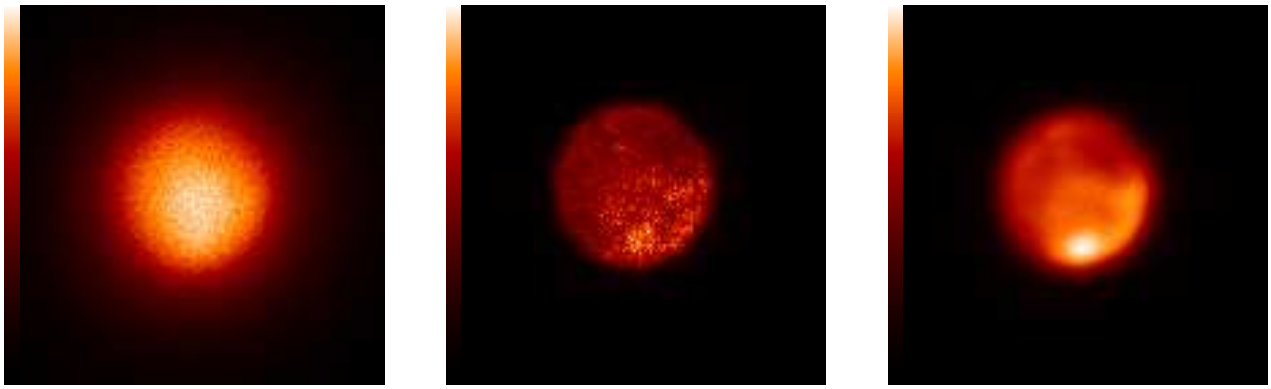

Corrected Image | Richardson-Lucy (3000 it.) | Richardson-Lucy (200 it.)

Figure 9: Observation of Ganymede with ONERA's AO bench on 1997/09/28 at 20:18 UT. The imaging wavelength is $\lambda = 0.85\mu m$ and the exposure time 100 sec. The estimated total flux is $\approx 8.10^7 photons$. The estimated D/r_o is 23 and the resulting Strehl Ratio of the order of 5%. The total field of view for the deconvolution is 7.9 arcsec but only the central 3.80 arcsec field of view is printed here. We show the corrected image and two estimates obtained with the RL algorithm interrupted respectively at 3000 and 200 iterations.

the mean PSF and the results are shown in Fig. 9. With a large number of iterations the algorithm tends towards the ML solution which is very noisy. Stopping the algorithm before convergence limits the amplification of noise and gives a low resolution estimate. Here, at 200 iterations, only high contrast large scale structures are visible (upper right dark area and lower bright spot). A major drawback is that there is no objective criterion to determine an "optimal" number of iterations. The edge preserving myopic deconvolution is shown in Fig. 10. The contour

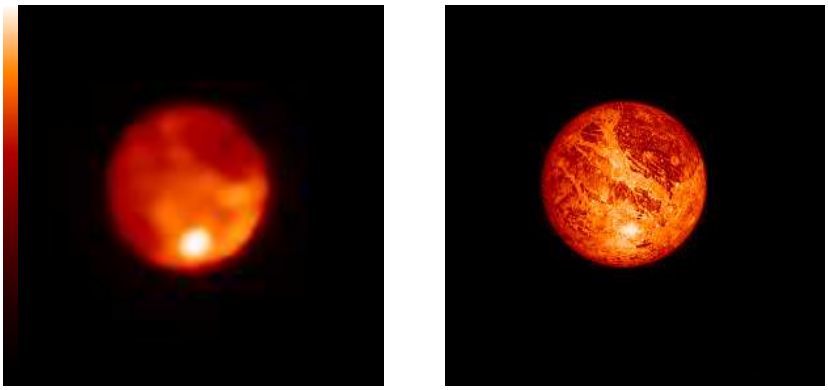

Myopic Deconvolution

JPL data base

Courtesy NASA/JPL/Caltech

Figure 10: Edge preserving myopic deconvolution of the image of Ganymede shown in Fig. 9. A broad band image obtained from a NASA/JPL data base is shown for comparison [see http://space.jpl.nasa.gov/]

is much sharper. Many details are seen on the surface and can be compared to the high resolution map obtained from the NASA/JPL data base gathering probe images. The main features are well restored (various dark areas, bright spot). Note that the myopic deconvolution gives a much better restoration of the lower bright spot (shape and position) than the 200 iteration RL estimate.

5 Conclusion

We have presented a MAP-based myopic restoration scheme with an application to AO images of solar system objects. We have shown how to account for the PSF variability due to seeing variations through the use of a specific regularization term. We have also tested an edge preserving object prior which gives a better photometric accuracy than classical linear schemes when deconvolving planetary-like objects. The myopic deconvolution has been applied to Vesta's images showing the rotation of the asteroid and the associated albedo variations. The deconvolution of an image of Ganymede gives a very good restoration of its surface structures which are compared to a NASA probe image data base.

6 Acknowledgments

This work was supported by contracts from Service Technique des Technologies Communes, Ministère de la Défense, France. The authors thank Guy Le Besnerais, Jean-Pierre Véran, Clélia Robert, Jean-Luc Beuzit and Gérard Rousset for many fruitful discussions. Many thanks also to Pierre-Yves Madec, Didier Rabaud, Bruno Fleury, Joseph Montri, Francis Mendez, François Charbonnier, Laurent Rousset-Rouvière, Caroline Dessenne, who made this AO bench happen and participated to the observing run. Thanks to E. C. Downey for releasing `Xephem` which was very useful for the preparation of the observations.

References

[1] A. Labeyrie, "Attainment of diffraction-limited resolution in large telescopes by Fourier analysing speckle patterns," Astron. Astrophys. **6,** 85–87 (1970).

[2] K. T. Knox and B. J. Thompson, "Recovery of images from atmospherically degraded short exposure photographs," Astrophys. J. Lett. **193,** L45–L48 (1974).

[3] G. Weigelt, "Modified astronomical speckle interferometry "speckle masking"," Opt. Commun. **21,** 55–59 (1977).

[4] J. Primot, G. Rousset, and J.-C. Fontanella, "Deconvolution from wavefront sensing: a new technique for compensating turbulence-degraded images," J. Opt. Soc. Am. A **7,** 1598–1608 (1990).

[5] J. W. Hardy, J. E. Lefevbre, and C. L. Koliopoulos, "Real time atmospheric compensation," J. Opt. Soc. Am. **67,** 360–369 (1977).

[6] G. Rousset, J.-C. Fontanella, P. Kern, P. Gigan, F. Rigaut, P. Léna, C. Boyer, P. Jagourel, J.-P. Gaffard, and F. Merkle, "First diffraction-limited astronomical images with adaptive optics," Astron. Astrophys. **230,** 29–32 (1990).

[7] F. Rigaut, G. Rousset, P. Kern, J.-C. Fontanella, J.-P. Gaffard, F. Merkle, and P. Léna, "Adaptive optics on a 3.6-m telescope : results and performance," Astron. Astrophys. **250,** 280–290 (1991).

[8] M. C. Roggemann and C. L. Matson, "Power spectrum and Fourier phase spectrum estimation by using fully and partially compensating adaptive optics and bispectrum postprocessing," J. Opt. Soc. Am. A **9,** 1525–1535 (1992).

[9] J. M. Conan, P. Y. Madec, and G. Rousset, "Image formation in adaptive optics partial correction," in *Active and Adaptive Optics*, (Garching, Germany, 1993).

[10] J.-M. Conan, "Étude de la correction partielle en optique adaptative," Ph.D. thesis, Université Paris XI Orsay, 1994.

[11] E. Tessier, "Image quality with current adaptive optics instruments," Astron. Astrophys. Suppl. Ser. **125,** 581–593 (1997).

[12] J. C. Christou, "Deconvolution of adaptive optics images," in *these proceedings (ESO/OSA topical meeting on astronomy with adaptive optics present results and future programs)*, (1998).

[13] T. Fusco, J.-P. Véran, J.-M. Conan, and L. Mugnier, "Myopic deconvolution method for adaptive optics images of stellar fields," Astron. Astrophys. Suppl. Ser. **133,** 1–10 (1998).

[14] J. D. Drummond, R. Q. Fugate, and J. C. Christou, "Full Adaptive Optics Images of Asteroids Ceres and Vesta Rotational Poles and Triaxial Ellipsoid Dimensions," Icarus (1997), submitted.

[15] D. M. Titterington, "General structure of regularization procedures in image reconstruction," Astron. Astrophys. **144,** 381–387 (1985).

[16] G. Demoment, "Image Reconstruction and Restoration: Overview of Common Estimation Structures and Problems," IEEE Trans. Acoust. Speech Signal Process. **37,** 2024–2036 (1989).

[17] W. H. Richardson, "Bayesian-based iterative method of image restoration," J. Opt. Soc. Am. **62,** 55–59 (1972).

[18] L. B. Lucy, "An iterative technique for rectification of observed distributions," Astrophys. J. **79,** 745–754 (1974).

[19] J.-P. Véran, "Estimation de la réponse impulsionnelle et restauration d'image en optique adaptative Application au système d'optique adaptative du Télescope Canada-France-Hawaii," Ph.D. thesis, Ecole Nationale Supérieure des Télécommunications, 1997.

[20] J.-M. Conan, L. M. Mugnier, T. Fusco, V. Michau, and G. Rousset, "Myopic Deconvolution of Adaptive Optics Images using Object and Point Spread Function Power Spectra," Appl. Opt. **37,** 4614–4622 (1998).

[21] L. M. Mugnier, J.-M. Conan, T. Fusco, and V. Michau, "Joint Maximum a Posteriori Estimation of Object and PSF for Turbulence Degraded Images," in *Bayesian Inference for Inverse problems*, **3459,** 50–61 (San Diego, CA (USA), 1998).

[22] H. L. Van Trees, *Detection, Estimation, and Modulation Theory* (John Wiley & Sons, New York, 1968).

[23] P. J. Green, "Bayesian Reconstructions from Emission Tomography Data Using a Modified EM Algorithm," IEEE Trans. Med. Imag. **9,** 84–93 (1990).

[24] C. Bouman and K. Sauer, "A Generalized Gaussian Image Model for Edge-Preserving MAP Estimation," IEEE Trans. Image Processing **2,** 296–310 (1993).

[25] S. Brette and J. Idier, "Optimized Single Site Update Algorithms for Image Deblurring," in *Proceedings of the International Conference on Image Processing*, pp. 65–68 (Lausanne, Switzerland, 1996).

[26] E. Thiébaut and J.-M. Conan, "Strict *a priori* constraints for maximum-likelihood blind deconvolution," J. Opt. Soc. Am. A **12,** 485–492 (1995).

[27] G. R. Ayers and J. C. Dainty, "Iterative blind deconvolution and its applications," Opt. Lett. **13,** 547–549 (1988).

[28] R. W. Gerchberg and W. O. Saxton, "A practical algorithm for the determination of phase from image and diffraction plane pictures," Optik **35,** 237–246 (1972).

[29] R. W. Gerchberg, "Super-resolution through error energy reduction," Opt. Acta **21,** 709–720 (1974).

[30] A. Papoulis, "A New Algorithm in Spectral Analysis and Band-Limited Extrapolation," IEEE Trans. Circuits Syst. **CS-22,** 735 (1975).

[31] A. Levi and H. Stark, "Restoration from Phase and Magnitude by Generalized Projections," *Image Recovery: Theory and Application*, H. Stark, ed., (Academic Press, 1987), Chap. 8, pp. 277–320.

[32] T. J. Holmes, "Blind deconvolution of speckle images quantum-limited incoherent imagery: maximum-likehood approach," J. Opt. Soc. Am. A **9,** 1052– 1061 (1992).

[33] R. G. Lane, "Blind deconvolution of speckle images," J. Opt. Soc. Am. A **9,** 1508–1514 (1992).

[34] T. J. Schultz, "Multiframe blind deconvolution of astronomical images," J. Opt. Soc. Am. A **10,** 1064–1073 (1993).

[35] S. M. Jefferies and J. C. Christou, "Restoration of astronomical images by iterative blind deconvolution," Astrophys. J. **415,** 862–874 (1993).

[36] R. G. Lane, "Methods for maximum-likelihood deconvolution," J. Opt. Soc. Am. A **13,** 1992–1998 (1996).

[37] J. C. Christou, D. Bonaccini, and N. Ageorges, "Deconvolution of Adaptive Optics Near-Infrared System (ADONIS) Images," in *Adaptive Optics and Applications*, R. K. Tyson and R. Q. Fugate, eds.,**3126,** 68–80 (Soc. Photo-Opt. Instrum. Eng., Washington, 1997).

[38] D. G. Sheppard, B. R. Hunt, and M. W. Marcellin, "Iterative multiframe superresolution algorithms for atmospheric-turbulence-degraded imagery," J. Opt. Soc. Am. A **15,** 978–992 (1998).

[39] Y.-L. You and M. Kaveh, "A Regularization Approach to Joint Blur Identification and Image Restoration," IEEE Trans. Image Processing **5,** 416–428 (1996).

[40] J.-P. Véran, F. Rigaut, H. Maître, and D. Rouan, "Estimation of the adaptive optics long exposure point spread function using control loop data," J. Opt. Soc. Am. A **14,** 3057–3069 (1997).

[41] C. Dumas and O. R. Hainaut, "Mapping Vesta in the Visible and Near-Infrared: the 1994 and 1996 Oppositions as Viewed from the Ground," in *Workshop on Evolution of Igneous Asteroids: Focus on Vesta and the HED Meteorites*, D. W. Mittlefehldt and J. J. Papike, eds.,**Lunar and Planetary Institute Tech. Rpt. 96-02(1),** 7–8 (Lunar and Planetary Institute, Houston (USA), 1996).

[42] C. Dumas and O. R. Hainaut, "Mapping Vesta with Adaptive Optics: the 1996 Opposition," Bulletin of the American Astronomical Society **28,** 1101 (1996), Division for Planetary Science Meeting.